Optimization of the thermoelectric power factor: Coupling between chemical order and transport properties

Mattias Ångqvist, Daniel O. Lindroth, and Paul Erhart*

Chalmers University of Technology, Department of Physics, S-412 96 Gothenburg, Sweden

E-mail: erhart@chalmers.se

Abstract

Many thermoelectric materials are multi-component systems that exhibit chemical ordering, which can affect both thermodynamic and transport properties. Here, we address the coupling between order and thermoelectric performance in the case of a prototypical inorganic clathrate ($Ba_8Ga_{16}Ge_{30}$) using a combination of density functional and Boltzmann transport theory as well as alloy cluster expansions and Monte Carlo simulations. The calculations describe the experimentally observed site occupancy factors and reproduce experimental data for the transport coefficients. By inverting the cluster expansion we demonstrate that the power factor can be increased by more than 60% for certain chemical ordering patterns that involve reducing the number of the trivalent species on the 6*c* Wyckoff site. This enhancement is traced to specific features of the electronic band structure. The approach taken in the present work can be readily adapted to other materials and enables a very general form of band structure engineering. In this fashion it can guide the computational design of compounds with optimal transport properties.

*To whom correspondence should be addressed

1 Introduction

Thermoelectric materials allow one to extract electrical currents from thermal gradients and vice versa.[1,2] They have found applications in various areas including e.g., power generation in remote locations, waste heat recuperation, and active cooling. The thermodynamic efficiency of the conversion process is quantified by the thermoelectric figure of merit zT. The latter depends on the Seebeck coefficient S, which measures the coupling strength between a thermal gradient and the generated potential difference, the electrical conductivity σ as well as the thermal conductivity κ according to

$$zT = TS^2\sigma/\kappa. \tag{1}$$

The $S^2\sigma$ term in the enumerator is known as the thermoelectric power factor.[3] While in efforts to increase zT it has received relatively less attention than the thermal conductivity κ,[4–7] several strategies for its enhancement have been proposed. The key challenge is that S and σ are anti-correlated in so far as the Seebeck coefficient usually decreases with carrier concentration whereas the electrical conductivity increases.[3] To mitigate this situation, Hicks and Dresselhaus suggested to reduce dimensionality by means of quantum well structures[8,9] while Mahan and Sofo showed conceptually that optimal conditions are obtained for a very narrow distribution of states with high group velocities.[10] These ideas were in fact later realized e.g., in the form of nanostructuring,[11–13] which also is useful for reducing the thermal conductivity, resonant levels,[3] and band structure engineering.[14–16] It is also worthwhile noting the extremely high power factors that were achieved at low temperatures in $FeSb_2$.[17,18] They have been attributed to strong electronic correlation resulting from the interplay between localization and partially occupied states.

While most of the aforementioned approaches have been devised in the context of "simple" lattice structures, many thermoelectric materials including e.g., skutterudites, inorganic clathrates as well as other Zintl compounds, and half-Heusler alloys[2] are multi-component

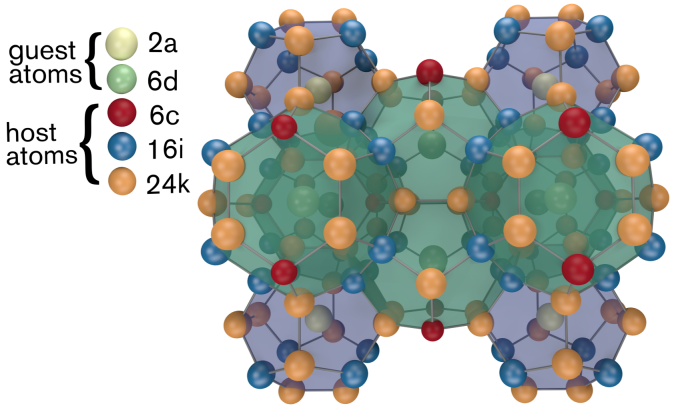

Figure 1: Crystal structure of type I clathrates. The guest species (Ba) occupies Wyckoff sites of type $2a$ and $6d$, while the host species (Ga, Ge) occupy Wyckoff sites of type $6c$, $16i$, and $24k$.

systems that exhibit some form of chemical order. Here, using the prototypical inorganic clathrate[19,20] $Ba_8Ga_{16}Ge_{30}$ (Fig. 1) as an example we demonstrate that the power factor can be enhanced by more than 60% by optimizing the chemical order. To this end, we first resolve the coupling between the chemical order and transport properties, in particular the power factor, and then employ an inverse design approach to identify the structure that maximizes the power factor. This approach yields a clear guideline for maximizing the power factor by structural optimization that we anticipate to be in principle transferable to other inorganic clathrates.

In this work we employ a combination of density functional theory (DFT) and Boltzmann transport theory (BTT) calculations with alloy cluster expansions (CE) and Monte Carlo (MC) simulations (Fig. 2). This approach is directly applicable to other materials that exhibit a variable chemical order. It thereby opens up the avenue for a more controlled and systematic design of structures with optimal transport properties that is not limited to thermoelectric materials.

The remainder of the paper is organized as follows. In the following section, we construct a model for the chemical order based on electronic structure calculations and describe the variation of the site occupancy factors with temperature. Using configurations that are

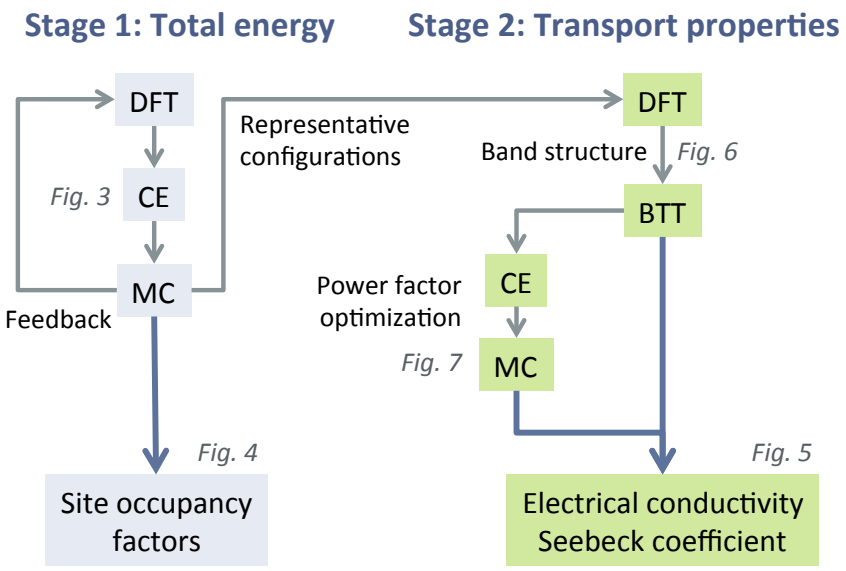

Figure 2: Schematic illustration of the relation between the methods employed in the present work. DFT: density functional theory; MC: Monte Carlo simulations; CE: alloy cluster expansion; BTT: Boltzmann transport theory.

representative for the chemical order at different temperatures, we then analyze the transport properties and construct a model that maps ordering patterns to the power factor at 900 K. This model is subsequently employed to determine the chemical ordering that maximizes the power factor.

2 Calculation methods

2.1 Chemical ordering

Density functional theory (DFT) calculations were carried out using the projector augmented wave method[21,22] as implemented in the Vienna ab-initio simulation package.[23,24] Exchange-correlation effects were treated within the generalized gradient approximation as parameterized by Perdew, Burke, and Ernzerhof (PBE).[25] A set of 200 structures based on the 54-atom primitive unit cell was created by randomly assigning Ga and Ge atoms to different Wyckoff sites that comprise the host structure. A further set of 100 structures was created

in the same fashion but subject to the condition that Ga–Ga first-nearest neighbors were disallowed. For each structure both the ionic positions and the cell metric were fully relaxed until all atomic forces were less than 10 meV/Å and absolute stresses below 0.1 kbar. In these calculations the Brillouin zone was sampled using a Γ-centered $3 \times 3 \times 3$ $\boldsymbol{k}$-point mesh, the plane wave basis set was expanded up to a cutoff energy of 243 eV, and the electronic self-consistency loop was terminated if the change in the total energy dropped below 10^{-5} eV between consecutive iterations.

Subsequently, the DFT energy landscape as well as quantities such as the band gap and the power factor were represented by cluster expansions (CE) of the form[26,27]

$$A = A_0 + \sum_{\alpha} m_\alpha J_\alpha \bar{\Pi}_\alpha(\boldsymbol{\Sigma}), \tag{2}$$

where A denotes the respective quantity of interest and the summation runs over all symmetry distinct clusters (singlets, pairs, triplets ...). Each cluster has a multiplicity m_α and is associated with an effective cluster interaction (ECI) J_α. The cluster correlations $\bar{\Pi}_\alpha$ are computed as symmetrized averages of products over the pseudospin vector $\boldsymbol{\Sigma}$. The latter represents the lattice sites associated with the host matrix where $\Sigma = \pm 1$ for Ge and Ga, respectively.

The ECIs were obtained using the compressive sampling technique[28] adapted for CE construction.[29] The split Bregman algorithm[30,31] was employed to solve the optimization problem using parameters of $\mu = 0.001$ (which controls the sparseness of the solution) and $\lambda = 100$ (see Refs. 29,31 for details concerning the role of these parameters). A range of different values for μ and λ was tested. Within reasonable bounds (see e.g., Ref. 29), these parameters were found to have inconsequential effects on the results presented here.

Each CE was carefully tested with respect to its predictive power using both cross-validation and ground state searches. Due to the large number of different crystallographic sites there is a large number of distinct clusters, 3 singlets, 13 pairs and 26 triplets relative to

a 5 Å cutoff radius, respectively. These numbers are noticeably larger than for simpler structures such as face-centered cubic (see Fig. S7), whence the compressive sampling approach is particularly useful.[29]

The CEs were sampled using Monte Carlo (MC) simulations in the canonical ensemble. Supercells typically comprising $2 \times 2 \times 2$ unitcells were initialized at a temperature of 1200 K and then cooled down to 0 K at a rate of 50 K per MC cycle (1 MC cycle is equivalent to N trial moves, where N is the number of sites in the simulation). At each new temperature the system was first equilibrated for 50,000 MC cycles and then sampled for 100,000 MC cycles. The effect of supercell size on the SOFs is illustrated in Fig. S8.

2.2 Electrical transport properties

For several configurations the wave function of the fully relaxed structure was converged using a Γ-centered $4 \times 4 \times 4$ $\boldsymbol{k}$-point mesh, followed by a non self-consistent computation of the eigenenergy spectra on a Γ-centered $20 \times 20 \times 20$ mesh. Using the interpolated eigenenergy spectra and electronic group velocities the electrical conductivity and the Seebeck coefficient were computed using both an in-house and the BoltzTrap code[32] by evaluating the following expressions that are obtained within the relaxation time approximation to the Boltzmann transport equation[32–34]

$$\sigma = \frac{2e^2}{\Omega} \sum_{i\boldsymbol{k}} g_{\boldsymbol{k}} \boldsymbol{v}_{i\boldsymbol{k}} \otimes \boldsymbol{v}_{i\boldsymbol{k}} \tau_{i\boldsymbol{k}} \left(\frac{\partial f}{\partial \varepsilon} \right)_{\varepsilon = \varepsilon_{i\boldsymbol{k}}} \tag{3}$$

$$\mathbf{S} = \frac{\sigma^{-1}}{eT} \sum_{i\boldsymbol{k}} g_{\boldsymbol{k}} \boldsymbol{v}_{i\boldsymbol{k}} \otimes \boldsymbol{v}_{i\boldsymbol{k}} \tau_{i\boldsymbol{k}} \left[\varepsilon_{i\boldsymbol{k}} - \mu_e \right] \left(\frac{\partial f}{\partial \varepsilon} \right)_{\varepsilon = \varepsilon_{i\boldsymbol{k}}} . \tag{4}$$

Here, Ω is the unit cell volume, $g_{\boldsymbol{k}}$ is the $\boldsymbol{k}$-point weight, i refers to the band index, $\tau_{i\boldsymbol{k}}$ is the mode and momentum dependent lifetime, $\boldsymbol{v}_{i\boldsymbol{k}} = \hbar^{-1} \partial \varepsilon_{i\boldsymbol{k}} / \partial \boldsymbol{k}$ is the group velocity, f is the occupation function, and μ_e is the electron chemical potential. In the present work, the scattering time was assumed to be momentum and state independent as commonly done in calculations of this type.[32,34,35]

We note that semi-local exchange-correlation functionals such as the PBE functional used in the present work are known to systematically underestimate the band gap. This error can have a strong impact on the transport properties in weakly doped materials. In the present work we are, however, concerned with very high charge carrier concentrations as thermoelectrics are typically heavily (degenerately) doped semiconductors. As shown in Fig. S3, under these conditions the magnitude of the band gap (while assuming rigid bands) has a very small effect on the transport properties, whence the band gap underestimation is of minor concern for the present work.

As a further validation, we also carried out calculations for selected structures using the modified Becke-Johnson (mBJ) functional,[36,37] which yields much improved band gaps and band structures compared to PBE-DFT. The results (Fig. S4) demonstrate that, apart from an increase in the band gap, the conduction and valence band structure near the band edges are, however, very similar between PBE and mBJ-DFT, especially in the region that determines the transport properties under degenerate doping conditions. For all calculations reported below we therefore employ the PBE-DFT band structure.

3 Chemical ordering

Inorganic clathrates of type I, such as $Ba_8Ga_{16}Ge_{30}$, belong to space group[38] $Pm\bar{3}n$ (international tables of crystallography number 223) and feature two smaller and six larger cages per unit cell.[19,20,39] $Ba_8Ga_{16}Ge_{30}$ has been investigated extensively both experimentally[40–45] and theoretically,[35,41,46–48] especially because of its promising thermoelectric properties. Here, the host structure is composed of Ga and Ge atoms, which occupy $6c$, $16i$, and $24k$ Wyckoff sites (Fig. 1)[49] as revealed by experimental measurements of the site occupancy factors (SOFs).[39] Analysis of diffraction data yields for example Ga occupancies between 60 and 76% for the $6c$ site, which deviates considerably from the value of $\mathrm{Ga}/(\mathrm{Ga}+\mathrm{Ge}) = 16/(16+30) = 35\%$ corresponding to the nominal stoichiometry of the compound.[43] The experimental observations

have been condensed into a set of rules for the SOFs,[39] partially based on calculations,[46] which have shown that bonds between trivalent species, in the present case Ga atoms, are energetically unfavorable.

Here, in order to model the chemical order, we constructed an alloy CE based on a set of total energies for two hundred structures that were obtained from DFT calculations. The structures were generated by randomly assigning Ga and Ge atoms to lattice sites, while maintaining a ratio of 16:30. The number of structures can be compared to the total number of *possible* configurations, which, excluding symmetry, is close to 10^{12} for the 54-atom primitive unit cell. The CE nonetheless yields a very low cross-validation score of 0.9 meV/atom and excellent overall agreement with the reference data as illustrated by a juxtaposition of total energies from DFT and CE [Fig. 3(a)]. The final CE includes 3 singlet, 13 pair, and 24 triplet terms and is rather short ranged [Fig. 3(b)].

It must be noted that the stoichiometry of experimentally synthesized clathrates often deviates from the ideal ratio of 8:16:30 for Ba:Ga:Ge.[39,50] These effects can in fact be represented using the total energy CE used in the present work.[51] In the case of $Ba_8Ga_{16}Ge_{30}$ the variation of the SOFs with composition is, however, relatively weak and, as apparent from the comparison below, its description is not essential for achieving good agreement with experimental transport coefficients. The effect of composition on ordering will therefore be the topic of a separate publication.[51]

The temperature dependence of the Ga SOFs was extracted by sampling the total energy CE with Monte Carlo (MC) simulations [Fig. 4(a)]. From the data it is apparent that already close to the melting temperature the SOFs deviate strongly from the stoichiometric ratio, which would imply a value of $16/(16+30) = 35\%$, indicating that the configurational entropy does not entirely override the energy associated with ordering even at these temperatures. As the temperature is reduced the SOFs deviate more strongly from 35% as the chemical distribution is increasingly dictated by energy. The variation in the SOFs is primarily the result of the energy penalty on trivalent (Ga) first-nearest neighbor pairs that has been

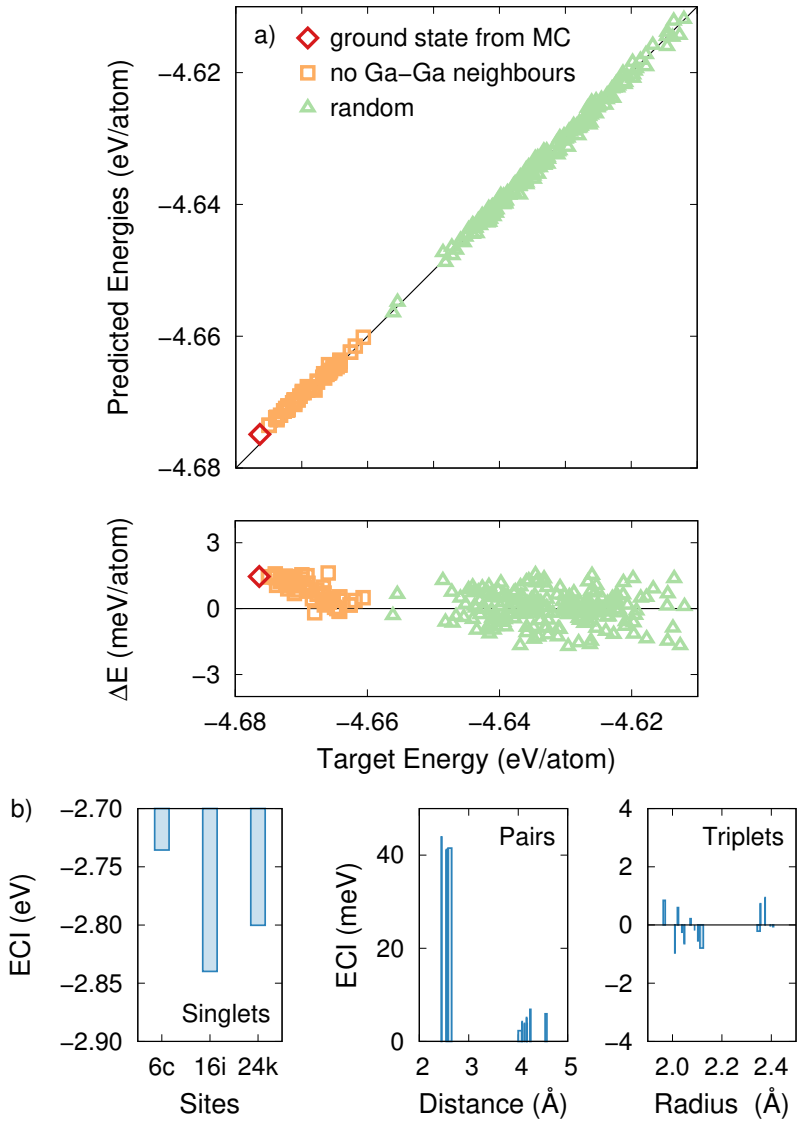

Figure 3: (a) Total energies obtained from cluster expansion (predicted) and electronic structure calculations (target). The data points shown by triangles were employed for constructing a cluster expansion for the total energy. Squares indicate data from structures without first-nearest neighbor Ga–Ga bonds, whereas diamonds represent the structure obtained via a simulated annealing procedure from MC simulations. (b) Effective cluster interactions (ECI) of the total energy cluster expansion as a function of cluster size.

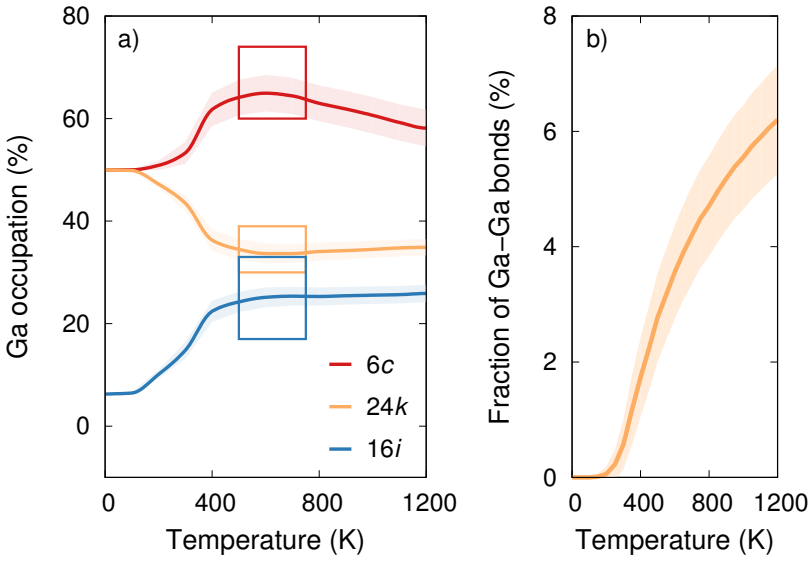

Figure 4: (a) Gallium site occupancy factors as a function of temperature from MC simulations using a $2 \times 2 \times 2$ supercell. The shaded regions indicate one standard deviation. The boxes represent the range of the experimental SOF data and roughly indicate the temperature range, over which the chemical order appears to be frozen during sample preparation. (b) Fraction of first-nearest Ga–Ga bonds as a function of temperature. For comparison, the average fraction of Ga-Ga bonds for a completely random structure is $c_{\mathrm{Ga}}^2 = 12.1\%$.

pointed out earlier[46] and is also apparent in the ECIs [Fig. 3(b)]. It is therefore logical that the number of Ga–Ga bonds monotonically decreases with decreasing temperature as shown in Fig. 4(b).

The experimentally observed SOF ranges are indicated by rectangles in Fig. 4(a). In experimental settings chemical ordering will at some temperature become kinetically hindered as it requires atomic rearrangement, which is a temperature activated process. The precise conditions, at which freezing of the chemical order occurs, are unknown whence a temperature window between 550 and 720 K has been indicated in Fig. 4(a). Within the indicated temperature range the agreement between experiment and model is actually excellent, supporting the present approach. The experimentally observed structure can thus be considered as a state of intermediate chemical order, which has been established during cooling as the result of slowing kinetics.

At low temperatures the system eventually reaches a fully ordered state with rhombo-

hedral symmetry (space group R3, ITC no. 146, see Table S1 for a compilation of the crystallographic parameters). As a further validation of the CE the total energy of this ordered state structure was calculated with DFT, which gave a value that deviates by less than 2 meV/atom from the CE value, demonstrating not only the accuracy but the predictive quality of the latter. This fact is even more remarkable given that the structures used for CE construction, which were obtained by random sampling, generally contain a much larger number of Ga–Ga bonds than the configurations observed during the MC simulations, even at temperatures close to the melting point.

The ordered configuration, from here on referred to as the ground state structure, is characterized by the absence of Ga–Ga bonds in the first neighbor shell and a minimal number of Ga–Ga bonds in the second and third shell. In addition it also minimizes the Ga SOF for Wyckoff site 16*i*.

4 Electrical transport properties

4.1 Comparison to experiment

The electrical transport properties of $Ba_8Ga_{16}Ge_{30}$ have been previously investigated using first-principles calculations employing either structures that were constructed using intuition and energy minimization[34,35,46] or the virtual crystal approximation.[47] Here, we therefore systematically discriminate the effect of thermally induced disorder on these properties. Specifically, we target *n*-type material, which is commonly associated with Ge-excess. In this section, we benchmark our structural model and establish two crucial parameters, namely the charge carrier density and the effective electronic lifetime, by comparing our calculations with experimental transport data for *n*-type $Ba_8Ga_{16}Ge_{30}$.[42,44,52–55]

Five representative configurations per temperature were extracted from MC simulations at 600, 900, and 1200 K, respectively. The average and standard deviation of the total energy of these configurations correspond to the energy distribution at the respective temperatures

sampled by MC simulations. In addition we considered ten random structures and the ground state structure. The electrical conductivity σ and the Seebeck coefficient S were computed within the framework of the Boltzmann transport equation[32] as described in above.

We first consider the Seebeck coefficient S [see Eq. (4)], which varies with the charge carrier concentration n_e [Fig. S1]. For $n_e = 3 \times 10^{20}\,\mathrm{cm}^{-3}$ the calculations for the MC generated structures agree well with the experimental data [Fig. 5(a)].[42,44,52,53] This charge carrier density in turn is in good agreement with previous estimates based on experimental data.[35,47] While the variation among the MC generated structures —regardless of the temperature they represent— is rather small, the results for the random structures —and to a lesser extent the ground state structure— differ more notably both in magnitude and the temperature at which S is extremal.

We note that with regard to the Seebeck coefficient, the temperature dependence in the experiments appears slightly more linear than in the calculations, which leads to some deviation at low temperatures. This behavior could be related to the assumption of a mode and momentum independent relaxation time (compare section on Calculation methods) and also affects the power factor (see below).

After having established the carrier density, which is kept constant at $n_e = 3 \times 10^{20}\,\mathrm{cm}^{-3}$ from this point onward, it is possible to assess the electrical conductivity σ [see Eq. (3)]. The electronic lifetimes were assumed to be mode and momentum independent $\tau_{\mathrm{eff}} \approx \tau_i(\boldsymbol{k})$ (see e.g., Refs. 32,34,35,46,47).[56] Since an explicit calculation of $\tau_i(\boldsymbol{k})$ for $Ba_8Ga_{16}Ge_{30}$ is computationally currently impractical, we use an effective lifetime model with a simple temperature dependence $\tau_{\mathrm{eff}} = \tau_{300}(300\,\mathrm{K}/T)^{1/2}$ to represent acoustic phonon (piezoelectric) scattering,[57] which using $\tau_{300} = 15\,\mathrm{fs}$ yields very good agreement with experimental data [Fig. 5(b)]. The thus obtained effective lifetime at 300 K is in fact very similar to values from previous studies (see e.g., Refs. 35,47), which, however, neglected the variation of τ with temperature. It is apparent that the electrical conductivity σ again shows only a modest variation among the MC structures.

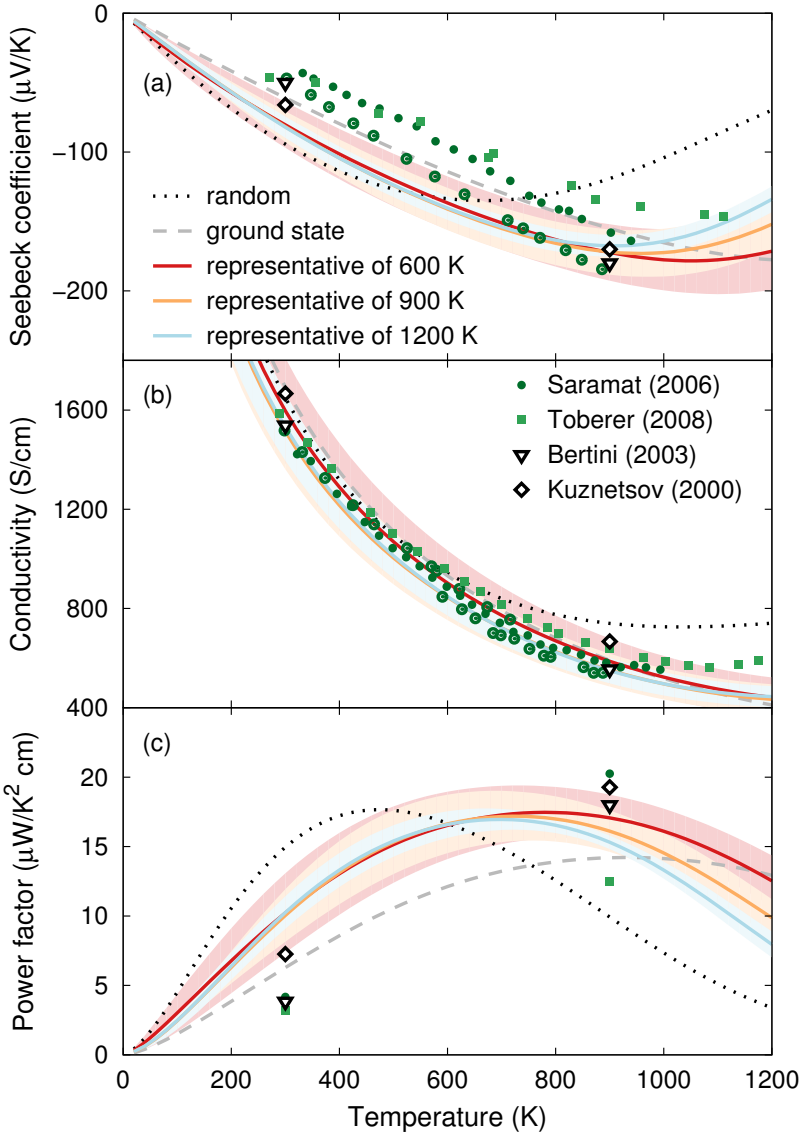

Figure 5: Electrical transport properties of n-type material at a carrier density of $3 \times 10^{20}\,\mathrm{cm}^{-3}$. (a) Seebeck coefficient, (b) electrical conductivity, and (c) power factor as a function of temperature from calculations in comparison with experimental data from Refs. 42,44,52,53. The degree of chemical order has a clear effect on the electrical transport properties as is evident by comparing the results from samples with a random distribution (dotted lines), the ground state structure (dashed lines), and configurations representative of the chemical order at 600 K (solid red), 900 K (solid orange), and 1200 K (solid blue). In the case of the MC generated structures the corresponding shaded areas represent one standard deviation.

Given the Seebeck coefficient S and the electrical conductivity σ we can now evaluate the power factor $S^2\sigma$, which most clearly highlights the effect of order on the electrical transport properties [Fig. 5(c)]. The MC generated structures yield power factors of 15 to 18 μW/K^{2}cm at 900 K, which agrees well with experimental data.[42,44,52,53] The maximum power factor occurs at approximately 800–900 K, which matches the range observed in most experiments. By comparison, the ground state (14 μW/K^{2}cm at 900 K) and random structures (9.6 $\pm$ 3.7 μW/K^{2}cm at 900 K) yield somewhat lower maxima. This suggests that the chemical ordering that is naturally established during synthesis corresponds to relatively optimal conditions with regard to the power factor, an observation that will be explored in detail below. Furthermore, we find that maximizing the power factor by variation of the charge carrier density n_e [Fig. S2] yield only a slight improvement of about 5%. This suggests that the experimental samples are already close to optimality with regard to n_e.

4.2 Order and electronic structure

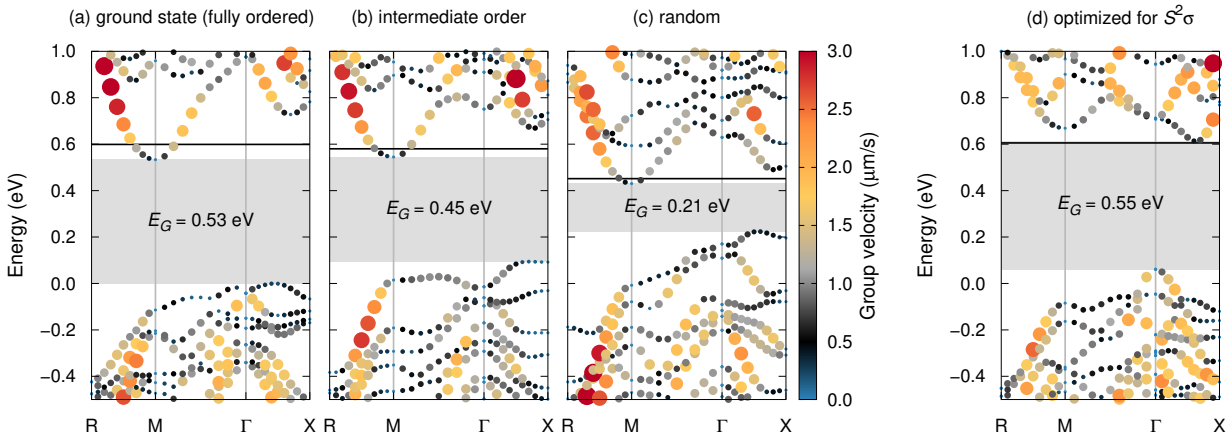

Figure 6: Effect of chemical order on the electronic structure. Band structures representing (a) the fully ordered ground state, (b) a configuration with intermediate order extracted from a MC simulation, (c) a random distribution, and (d) the structure optimized for maximum power factor at 900 K. The color scale and the size of the circles indicate the group velocity. The position of the Fermi level is shown by horizontal dashed lines. The energy scales of the different configurations were aligned using the Ba-1s states as described in Ref. 58 and the VBM of the ground state was arbitrarily set to zero.

The data presented above demonstrates that the power factor changes non-monotonically as a function of chemical order: The MC generated structures (intermediate level of order) exhibit on average higher power factors than both the ground state (highest degree of order) and the random structures (lowest degree of order). To resolve this behavior it is instructive to explore the effect of chemical order on the electronic structure as both Seebeck coefficient S and electrical conductivity σ are primarily determined by the electronic eigenenergies and group velocities, see Eqs. (3) and (4).

The electronic band structures of configurations representing different degrees of chemical order [Fig. 6] reveal that decreasing chemical order causes a systematic lowering of the band gap and a reduction in the dispersion of the lowermost conduction band level, which implies decreasing group velocities. With regard to the electrical conductivity σ, these two effects oppose each other as the $(\partial f/\partial\varepsilon)_{\varepsilon=\varepsilon_{i\boldsymbol{k}}}$ term in Eq. (3) increases with decreasing band gap, whereas smaller group velocities $\boldsymbol{v}_i(\boldsymbol{k})$ cause a reduction of the other term in the integrand. (In the widely adopted effective mass approximation, this is equivalent to asserting an increase in the charge carrier concentration and a reduction of the mobility due to a higher effective mass (smaller curvature), see e.g., Ref. 2). In the current case the two terms appear to largely cancel each other as the net effect of order on σ is comparably small [Fig. 5(b)].

To further resolve the coupling between order and the electrical transport properties, a closer inspection of the underlying band structures is instructive. To this end, we analyzed the mode resolved contributions to the power factor, which are most sensitive to the group velocity. It is found that for the ground state configuration the largest contribution to S stems from states in the vicinity of the M point, which is the location of the CBM [fully ordered, Fig. 6(a), $S^2\sigma = 14.2\,\mu\mathrm{W/K^2\,cm}$ at 900 K and $n_e = 3 \times 10^{20}/\mathrm{cm}^3$]. While in the case of intermediate chemical order the relative contribution of these states is reduced, higher lying states for example along the Γ-X direction are shifted downward and thus closer to the Fermi level providing a significantly larger contribution than in the case of the ground

state structure [Fig. 6(b), $S^2\sigma = 18.7\,\mu\mathrm{W/K^2\,cm}$]. The gain in the density of states in the vicinity of $\mu_e + k_B T$ outweighs the reduced dispersion (smaller group velocities) around the M-point and gives rise to a slight increase of the power factor relative to the ground state configuration. If the degree of chemical order is further reduced, the effect of an increase in the density of states near the Fermi energy levels off [Fig. 6(c), $S^2\sigma = 12.2\,\mu\mathrm{W/K^2\,cm}$] whereas level localization (and thus reduction of the group velocities) proceeds, causing the power factor to drop again.

The origin of the reduction of band gap and level of dispersion with decreasing chemical order can be understood by recalling some general principles from defect physics. The ground state structure represents a fully ordered structure whereas disordering can be thought of as the insertion of antisite defects.[59] As these are intrinsic defects with small lattice distortions the associated defect states are hybridized with band states, see e.g., Refs. 3,60,61; yet the associated levels are to some extent localized. In $Ba_8Ga_{16}Ge_{30}$ (and similar systems) the formation energies for such antisites are obviously very small, whence defect concentrations are easily in the percent range and the collective effect on the band structure becomes significant.

4.3 Power factor optimized structures

To substantiate the above argumentation, additional CEs were constructed for the band gap E_G as well as the power factor at 900 K ($n_e = 3 \times 10^{20}/\,\mathrm{cm^3}$), for which we obtained cross validation scores of 0.05 eV and $1.5\,\mu\mathrm{W/cmK^2}$, respectively. The CEs were subsequently sampled using MC simulations based on the CE for the total energy constructed earlier. Using the total energy as order parameter,[62] these simulations confirm for a large data sample that the band gap decreases monotonically with chemical disordering [Fig. 7(b)] whereas the power factor exhibits a maximum at a finite amount of disorder, which quite closely coincides with the *average* level of order between 600 and 1200 K.

Based on the CE for the power factor, we are now in a position to search for chemical

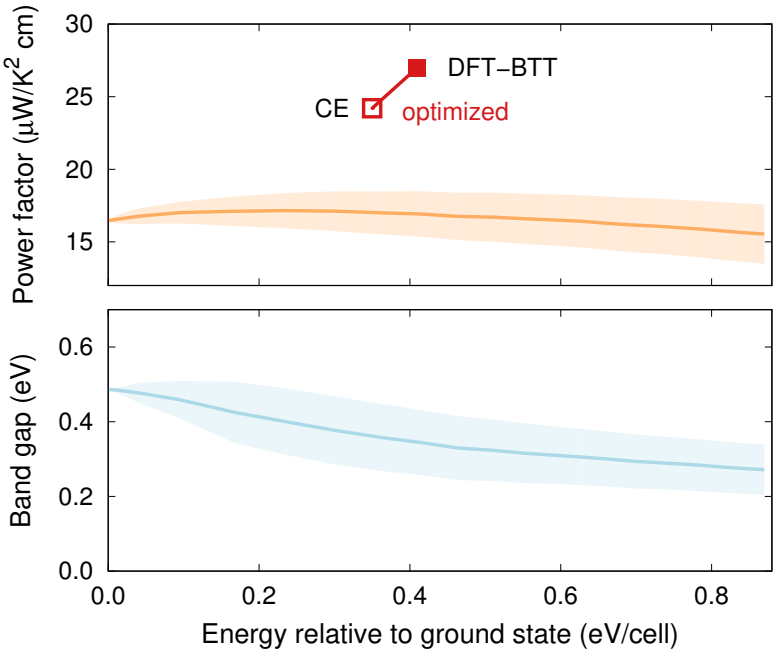

Figure 7: (a) Power factor and (b) band gap as a function of order (measured by the total energy) from MC-CE simulations. The maximum attainable power factor according to CE and DFT-BTT is indicated by red symbols. The shaded regions represent one standard deviation.

ordering patterns that maximize the power factor. To this end, simulated annealing runs were carried out on the landscape corresponding to $-S^2\sigma$ with an appropriate effective temperature scale. In this fashion several structures were obtained with predicted power factors of approximately $S^2\sigma = 24\,\mu\mathrm{W/K^2\,cm}$, which were confirmed by a subsequent DFT-BTT calculation yielding about $27\,\mu\mathrm{W/K^2\,cm}$ (Table S1).

The optimized structures are only about 8 meV/atom higher than the ground state structure, and thus energetically comparable to the structures obtained during the MC simulations described above. The most striking difference to both the ground state and MC generated representative structures described above is the redistribution of Ga occupation from the $6c$ to the $16i$ site (ground state structure: SOF($6c$)=50%; power factor optimized structure: SOF($6c$)=0%; see Table S1), whereas the average occupation of $24k$ sites is unaffected. In terms of the electronic structure this redistribution gives rise to a significantly higher density of states in the vicinity of the conduction band edge along with a notably larger contribution

from Ga atoms on $24k$ sites than in either the ground state or the MC generated structures (Fig. S6). Here, the vanishing Ga occupancy of $6c$ Wyckoff sites is a key feature as we generally find that larger power factors are correlated with a low $6c$ SOF.

It is now very instructive to analyze the features of the electronic structure that underlie the outstanding power factor of this configuration. A closer inspection of the band structure [Fig. 6(d)] reveals that unlike the other structures [Fig. 6(a-c)], all of which feature a CBM at the M-point, for the optimized structure the CBM is located along the Γ-X direction. This is the result of the lower energy of the corresponding states compared to the other structures. At the same time the high degree of order ensures that the configuration has a large band gap ($E_G = 0.55\,\mathrm{eV}$) comparable in magnitude to the ground state structure ($E_G = 0.54\,\mathrm{eV}$).

The integrand in the expression for the Seebeck coefficient Eq. (4) is maximal if the group velocity at approximately $\mu_e + 1.5 k_B T$ is large, which requires dispersed (delocalized) states. At the same time, it is desirable to have many states in this energy window, which would be achieved by localization (non-dispersed states). Since similar considerations apply to σ, optimizing $S^2\sigma$ thus tries to strike a balance between two diametrically opposed features. A three-dimensional visualization of the CBM [Fig. S5] shows that the optimized configuration achieves a large power factor by featuring multiple CBM pockets with large group velocities in the relevant energy range.

Similar features in the band structure involving "complex carrier pocket shapes" [63] were found to enhance thermoelectric performance also in other materials, see e.g., Refs. 14,16,63–65. The electronic structures that were observed in these cases can be thought of as realizations of the conditions formulated by Mahan and Sofo [10] according to which one seeks a narrow distribution of states near the Fermi level with high group velocities. While enhanced thermoelectric performance due the existence of multiple band extrema has been shown to be intrinsic to some materials, [64,65] it has been demonstrated that the relevant features can also be engineered by e.g., nanoinclusions, [14] careful selection of the components, [16] or volumetric band alignment via alloying. [63] The present results show that this level of band

structure engineering can even be accomplished by controlling the chemical order in a material. Furthermore, the present approach demonstrates that the identification of materials and compositions can be achieved using models that do not explicitly describe the electronic structure as long as they are properly trained with respect to higher level calculations.

5 Conclusions

In the present work, we used density functional theory calculations in conjunction with Monte Carlo simulations, alloy cluster expansions, and Boltzmann transport theory to investigate the coupling between chemical order and the electrical transport properties in the prototypical inorganic clathrate $Ba_8Ga_{16}Ge_{30}$.

The temperature dependence of the SOFs obtained from MC-CE simulations shows a strong asymmetry between different Wyckoff sites. The predicted SOFs in the temperature range between 550 and 720 K are in good agreement with experimental data. This observation provides a very sensible estimate for the temperature range, in which the chemical order is kinetically frozen in as the material cools down after synthesis. A simulated annealing procedure furthermore lead to a ground state structure that is primarily characterized by the absence of first-nearest neighbor Ga-Ga bonds.

Subsequently, the electrical conductivity σ and Seebeck coefficient S were computed for n-type conditions using a DFT-BTT approach for the ground state structure, a set of configurations representing the chemical order at different temperatures, as well as several random structures. The magnitude and temperature dependence of the Seebeck coefficient calculated for the representative structures at an electron concentration of $n_e = 3 \times 10^{20}/\mathrm{cm}^3$ was shown to match experimental data. Using a minimal model for the electronic lifetime based on scattering by acoustic phonons, we then achieved close agreement between experiment and calculations for both the electrical conductivity σ and power factor $S^2\sigma$. Thus equipped, the relation between chemical order and the power factor was scrutinized. It was shown that

the power factor exhibits a non-monotonic dependence on order (and temperature) with its average value exhibiting a maximum roughly in the range found in previous experiments.

Using a direct combination of DFT-BTT and MC-CE, we then identified structural motifs that maximize the power factor. Specifically, it was demonstrated that this can be achieved by minimizing the Ga SOF for 6*c* Wyckoff sites, which gives yields calculated power factors up to 27 μW/K^{2}cm corresponding to an improvement of about 60% compared to the "normal" order. The enhancement can be traced to an increase in the density of states near the conduction band edge with only a small reduction in the group velocities.

It is beyond the scope of this work to provide a recipe for synthesizing the exact structure in question but the relatively small energy cost associated with the depopulation of the 6*c* site suggests that it is thermodynamically within reach. It is for example possible that alloyed clathrates[66–69] provide means to control order more consciously, albeit at the cost of a much more complex parameter range. Other materials that exhibit partial ordering/disordering such as the cobaltates and skutterudites, Zintl compounds as well as complex alloys[2,16,70–75] can be anticipated to exhibit similar features and thus also warrant further study.

Here, modeling and simulation could provide useful guidance for navigating the complex and multidimensional composition space. In this context the approach utilized in the present work, which combines electronic structure calculations of transport properties with machine learning protocols, could prove to be highly useful for band structure engineering. In this fashion it can guide the computational design of compounds with optimal transport properties.

Associated content

Additional crystallographic information for the ground state structure as well as the power factor optimized structure in CIF format; a table with additional information for the two structures; supplementary figures documenting the temperature, doping level, and carrier

density dependence of Seebeck coefficient and power factor, the sensitiviy of the band structure to the exchange-correlation functional, the structure and composition of the band egdes, the number of ECIs as a function of cluster size, as well as the convergence of the SOFs with supercell size.

Acknowledgments

We are grateful to Anders Palmqvist and Richard Hejl for many helpful discussions. This work was funded by the Knut and Alice Wallenberg Foundation and the Swedish Research Council, and supported by computer time allocations by the Swedish National Infrastructure for Computing at NSC (Linköping) and PDC (Stockholm).

Notes and References

(1) Rowe, D., Ed. *Thermoelectrics Handbook: Macro to Nano*; CRC Press, 2005.

(2) Snyder, G. J.; Toberer, E. S. Complex thermoelectric materials. *Nature Mater.* **2008**, *7*, 105–114.

(3) Heremans, J. P.; Wiendlocha, B.; Chamoire, A. M. Resonant levels in bulk thermoelectric semiconductors. *Energy Environ. Sci.* **2012**, *5*, 5510–5530.

(4) Feldman, J. L.; Singh, D. J.; Kendziora, C.; Mandrus, D.; Sales, B. C. Lattice dynamics of filled skutterudites: La(Fe,Co)_4Sb_12. *Phys. Rev. Lett.* **2003**, *68*, 094301.

(5) Garg, J.; Bonini, N.; Kozinsky, B.; Marzari, N. Role of Disorder and Anharmonicity in the Thermal Conductivity of Silicon-Germanium Alloys: A First-Principles Study. *Phys. Rev. Lett.* **2011**, *106*, 045901.

(6) Biswas, K.; He, J.; Zhang, Q.; Wang, G.; Uher, C.; Dravid, V. P.; Kanatzidis, M. G.

Strained endotaxial nanostructures with high thermoelectric figure of merit. *Nature Chem.* **2011**, *3*, 160–166.

(7) Biswas, K.; He, J.; Blum, I. D.; Wu, C.-I.; Hogan, T. P.; Seidman, D. N.; Dravid, V. P.; Kanatzidis, M. G. High-performance bulk thermoelectrics with all-scale hierarchical architectures. *Nature* **2012**, *489*, 414–418.

(8) Hicks, L. D.; Dresselhaus, M. S. Effect of quantum-well structures on the thermoelectric figure of merit. *Phys. Rev. B* **1993**, *47*, 12727–12731.

(9) Heremans, J. P.; Dresselhaus, M. S.; Bell, L. E.; Morelli, D. T. When thermoelectrics reached the nanoscale. *Nature Nanotechn.* **2013**, *8*, 471–473.

(10) Mahan, G. D.; Sofo, J. O. The best thermoelectric. *Proc. Nat. Acad. Sci.* **1996**, *93*, 7436–7439.

(11) Heremans, J. P.; Thrush, C. M.; Morelli, D. T. Thermopower enhancement in PbTe with Pb precipitates. *J. Appl. Phys.* **2005**, *98*, 063703–063703–6.

(12) Heremans, J. P.; Jovovic, V.; Toberer, E. S.; Saramat, A.; Kurosaki, K.; Charoenphakdee, A.; Yamanaka, S.; Snyder, G. J. Enhancement of Thermoelectric Efficiency in PbTe by Distortion of the Electronic Density of States. *Science* **2008**, *321*, 554–557.

(13) Faleev, S. V.; Léonard, F. Theory of enhancement of thermoelectric properties of materials with nanoinclusions. *Phys. Rev. B* **2008**, *77*, 214304.

(14) Zhao, L.-D.; Dravid, V. P.; Kanatzidis, M. G. The panoscopic approach to high performance thermoelectrics. *Energy Environ. Sci.* **2013**, *7*, 251–268.

(15) Zhao, L.-D.; Tan, G.; Hao, S.; He, J.; Pei, Y.; Chi, H.; Wang, H.; Gong, S.; Xu, H.; Dravid, V. P.; Uher, C.; Snyder, G. J.; Wolverton, C.; Kanatzidis, M. G. Ultrahigh power factor and thermoelectric performance in hole-doped single-crystal SnSe. *Science* **2016**, *351*, 141–144.

(16) Bilc, D. I.; Hautier, G.; Waroquiers, D.; Rignanese, G.-M.; Ghosez, P. Low-Dimensional Transport and Large Thermoelectric Power Factors in Bulk Semiconductors by Band Engineering of Highly Directional Electronic States. *Phys. Rev. Lett.* **2015**, *114*, 136601.

(17) Bentien, A.; Madsen, G. K. H.; Johnsen, S.; Iversen, B. B. Experimental and theoretical investigations of strongly correlated $FeSb_{2-x}Sn_x$. *Phys. Rev. B* **2006**, *74*, 205105.

(18) Bentien, A.; Johnsen, S.; Madsen, G. K. H.; Iversen, B. B.; Steglich, F. Colossal Seebeck coefficient in strongly correlated semiconductor $FeSb_2$. *Europhysics Letters (EPL)* **2007**, *80*, 17008.

(19) Rogl, P. *Thermoelectrics Handbook*; CRC Press, 2005; Chapter 32, pp 1–24.

(20) Shevelkov, A. V.; Kovnir, K. In *Zintl Phases*; Fässler, T. F., Ed.; Structure and Bonding 139; Springer Berlin Heidelberg, 2011; pp 97–142.

(21) Blöchl, P. E. Projector augmented-wave method. *Phys. Rev. B* **1994**, *50*, 17953 –17979.

(22) Kresse, G.; Joubert, D. From ultrasoft pseudopotentials to the projector augmented-wave method. *Phys. Rev. B* **1999**, *59*, 1758 – 1775.

(23) Kresse, G.; Hafner, J. Ab initio molecular dynamics for liquid metals. *Phys. Rev. B* **1993**, *47*, 558–561.

(24) Kresse, G.; Furthmüller, J. Efficiency of ab-initio total energy calculations for metals and semiconductors using a plane-wave basis set. *Comput. Mater. Sci.* **1996**, *6*, 15–50.

(25) Perdew, J. P.; Burke, K.; Ernzerhof, M. Generalized Gradient Approximation Made Simple. *Phys. Rev. Lett.* **1996**, *77*, 3865–3868, erratum, *ibid.* **78**, 1396(E) (1997).

(26) Sanchez, J. M.; Ducastelle, F.; Gratias, D. Generalized cluster description of multicomponent systems. *Physica* **1984**, *128*, 334.

(27) Sanchez, J. M. Cluster expansion and the configurational theory of alloys. *Phys. Rev. B* **2010**, *81*, 224202.

(28) Candes, E.; Wakin, M. An Introduction To Compressive Sampling. *Signal Processing Magazine, IEEE* **2008**, *25*, 21 –30.

(29) Nelson, L. J.; Hart, G. L. W.; Zhou, F.; Ozolins, V. Compressive sensing as a new paradigm for model building. *Phys. Rev. B* **2013**, *87*, 035125.

(30) Yin, W.; Osher, S.; Goldfarb, D.; Darbon, J. Bregman Iterative Algorithms for l_1-Minimization with Applications to Compressed Sensing. *SIAM Journal on Imaging Sciences* **2008**, *1*, 143–168.

(31) Goldstein, T.; Osher, S. The Split Bregman Method for L1-Regularized Problems. *SIAM Journal on Imaging Sciences* **2009**, *2*, 323–343.

(32) Madsen, G. K.; Singh, D. J. BoltzTraP. A code for calculating band-structure dependent quantities. *Comp. Phys. Comm.* **2006**, *175*, 67–71.

(33) Ziman, J. M. *Electrons and phonons*; Clarendon Press: Oxford, 1960.

(34) Blake, N. P.; Møllnitz, L.; Kresse, G.; Metiu, H. Why clathrates are good thermoelectrics: A theoretical study of $Sr_8Ga_{16}Ge_{30}$. *J. Chem. Phys.* **1999**, *111*, 3133.

(35) Blake, N. P.; Latturner, S.; Bryan, J. D.; Stucky, G. D.; Metiu, H. Band structures and thermoelectric properties of the clathrates $Ba_8Ga_{16}Ge_{30}$, $Sr_8Ga_{16}Ge_{30}$, $Ba_8Ga_{16}Si_{30}$, and $Ba_8In_{16}Sn_{30}$. *J. Chem. Phys.* **2001**, *115*, 8060.

(36) Becke, A. D.; Johnson, E. R. A simple effective potential for exchange. *J. Chem. Phys.* **2006**, *124*, 221101.

(37) Tran, F.; Blaha, P. Accurate Band Gaps of Semiconductors and Insulators with a Semilocal Exchange-Correlation Potential. *Phys. Rev. Lett.* **2009**, *102*, 226401.

(38) Symmetry analyses were carried out using the SPGLIB library written by A. Togo, http://atztogo.github.io/spglib.

(39) Christensen, M.; Johnsen, S.; Iversen, B. B. Thermoelectric clathrates of type I. *Dalton Trans.* **2010**, *39*, 978–992.

(40) Sales, B. C.; Chakoumakos, B. C.; Jin, R.; Thompson, J. R.; Mandrus, D. Structural, magnetic, thermal, and transport properties of $X_8Ga_{16}Ge_{30}$ (X=Eu, Sr, Ba) single crystals. *Phys. Rev. B* **2001**, *63*, 245113.

(41) Bryan, J. D.; Blake, N. P.; Metiu, H.; Stucky, G. D.; Iversen, B. B.; Poulsen, R. D.; Bentien, A. Nonstoichiometry and chemical purity effects in thermoelectric $Ba_8Ga_{16}Ge_{30}$ clathrate. *Journal of Applied Physics* **2002**, *92*, 7281–7290.

(42) Saramat, A.; Svensson, G.; Palmqvist, A. E. C.; Stiewe, C.; Mueller, E.; Platzek, D.; Williams, S. G. K.; Rowe, D. M.; Bryan, J. D.; Stucky, G. D. Large thermoelectric figure of merit at high temperature in Czochralski-grown clathrate $Ba_8Ga_{16}Ge_{30}$. *J. Appl. Phys.* **2006**, *99*, 023708.

(43) Christensen, M.; Lock, N.; Overgaard, J.; Iversen, B. B. Crystal Structures of Thermoelectric n- and p-type $Ba_8Ga_{16}Ge_{30}$ Studied by Single Crystal, Multitemperature, Neutron Diffraction, Conventional X-ray Diffraction and Resonant Synchrotron X-ray Diffraction. *J. Am. Chem. Soc.* **2006**, *128*, 15657–15665.

(44) Toberer, E. S.; Christensen, M.; Iversen, B. B.; Snyder, G. J. High temperature thermoelectric efficiency in $Ba_8Ga_{16}Ge_{30}$. *Phys. Rev. B* **2008**, *77*, 075203.

(45) Cederkrantz, D.; Saramat, A.; Snyder, G. J.; Palmqvist, A. E. C. Thermal stability and thermoelectric properties of p-type $Ba_8Ga_{16}Ge_{30}$ clathrates. *J. Appl. Phys.* **2009**, *106*, 074509.

(46) Blake, N. P.; Bryan, D.; Latturner, S.; Møllnitz, L.; Stucky, G. D.; Metiu, H. Structure and stability of the clathrates $Ba_8Ga_{16}Ge_{30}$, $Sr_8Ga_{16}Ge_{30}$, $Ba_8Ga_{16}Si_{30}$, and $Ba_8In_{16}Sn_{30}$. *J. Chem. Phys.* **2001**, *114*, 10063–10074.

(47) Madsen, G. K. H.; Schwarz, K.; Blaha, P.; Singh, D. J. Electronic structure and transport in type-I and type-VIII clathrates containing strontium, barium, and europium. *Phys. Rev. B* **2003**, *68*, 125212.

(48) Madsen, G. K. H.; Santi, G. Anharmonic lattice dynamics in type-I clathrates from first-principles calculations. *Phys. Rev. B* **2005**, *72*, 220301.

(49) Eisenmann, B.; Schäfer, H.; Zagler, R. Die Verbindungen $A^{\mathrm{II}}_8 B^{\mathrm{III}}_{16} B^{\mathrm{IV}}_{30}$ (A^{II} = Sr, Ba; B^{III}= Al, Ga; B^{IV} = Si, Ge, Sn) und ihre Käfigstrukturen. *Journal of the Less Common Metals* **1986**, *118*, 43–55.

(50) Christensen, M.; Iversen, B. B. Host Structure Engineering in Thermoelectric Clathrates. *Chem. Mater.* **2007**, *19*, 4896.

(51) Ångqvist, M.; Erhart, P. in preparation.

(52) Bertini, L. et al. Thermoelectric performance of large single crystal clathrate $Ba_8Ga_{16}Ge_{30}$. *International Conference on Thermoelectrics Proceedings* **2003**, 127.

(53) Kuznetsov, V. L.; Kuznetsova, L. A.; Kaliazin, A. E.; Rowe, D. M. Preparation and thermoelectric properties of $A^{\mathrm{II}}_8 B^{\mathrm{III}}_{16} B^{\mathrm{IV}}_{30}$ clathrate compounds. *Journal of Applied Physics* **2000**, *87*, 7871–7875.

(54) Okamoto, N. L.; Kishida, K.; Tanaka, K.; Inui, H. Crystal structure and thermoelectric properties of type-I clathrate compounds in the BaGaGe system. *Journal of Applied Physics* **2006**, *100*, 073504.

(55) Okamoto, N. L.; Kishida, K.; Tanaka, K.; Inui, H. Effect of In additions on the thermoelectric properties of the type-I clathrate compound $Ba_8Ga_{16}Ge_{30}$. *Journal of Applied Physics* **2007**, *101*, 113525.

(56) Note that in general, one also requires the electronic lifetimes for computing the Seebeck coefficient. This dependence, however, vanishes if the lifetime is assumed to be momentum and mode independent.

(57) Yu, P. Y.; Cardona, M. *Fundamentals of Semiconductors*, 4th ed.; Springer: Berlin, 2001; chapter 5.2.

(58) Pfeifer, V.; Erhart, P.; Li, S.; Rachut, K.; Morasch, J.; Brötz, J.; Reckers, P.; Mayer, T.; Rühle, S.; Zaban, A.; Mora Seró, I.; Bisquert, J.; Jaegermann, W.; Klein, A. Energy Band Alignment between Anatase and Rutile TiO_2. *J. Phys. Chem. Lett.* **2013**, *4*, 4182–4187.

(59) Note that while other defects, most notably vacancies, are present in real materials, their numbers are relatively smaller than the number of such antisite defects. For simplicity they were therefore not considered in the present work.

(60) Lany, S.; Zunger, A. Assessment of correction methods for the band-gap problem and for finite-size effects in supercell defect calculations: Case studies for ZnO and GaAs. *Phys. Rev. B* **2008**, *78*, 235104.

(61) Erhart, P.; Åberg, D.; Lordi, V. Extrinsic point defects in aluminum antimonide. *Phys. Rev. B* **2010**, *81*, 195216.

(62) Order parameters are commonly used to describe phase transitions, which is, however, not the objective here. Rather we use the total energy merely as a convenient (single scalar) parameter to discriminate different structures by order.

(63) Bhattacharya, S.; Madsen, G. K. H. High-throughput exploration of alloying as design strategy for thermoelectrics. *Phys. Rev. B* **2015**, *92*, 085205.

(64) Usui, H.; Shibata, S.; Kuroki, K. Origin of coexisting large Seebeck coefficient and metallic conductivity in the electron doped $SrTiO_3$ and $KTaO_3$. *Phys. Rev. B* **2010**, *81*, 205121.

(65) Hao, S.; Shi, F.; Dravid, V. P.; Kanatzidis, M. G.; Wolverton, C. Computational Prediction of High Thermoelectric Performance in Hole Doped Layered GeSe. *Chem. Mater.* **2016**, *28*, 3218–3226.

(66) Christensen, M.; Johnsen, S.; Söndergaard, M.; Overgaard, J.; Birkedal, H.; Iversen, B. B. Fast Preparation and Characterization of Quarternary Thermoelectric Clathrates. *Chem. Mater.* **2009**, *21*, 122–127.

(67) Martin, J.; Erickson, S.; Nolas, G. S.; Alboni, P.; Tritt, T. M.; Yang, J. Structural and transport properties of $Ba_8Ga_{16}Si_xGe_{30-x}$ clathrates. *Journal of Applied Physics* **2006**, *99*, 044903.

(68) Martin, J.; Nolas, G. S.; Wang, H.; Yang, J. Thermoelectric properties of silicon-germanium type I clathrates. *Journal of Applied Physics* **2007**, *102*, 103719.

(69) Deng, S.; Tang, X.; Li, P.; Zhang, Q. High temperature thermoelectric transport properties of p-type $Ba_8Ga_{16}Al_xGe_{30-x}$ type-I clathrates with high performance. *J. Appl. Phys.* **2008**, *103*, 073503.

(70) Voneshen, D. J. et al. Suppression of thermal conductivity by rattling modes in thermoelectric sodium cobaltate. *Nature Mater.* **2013**, *12*, 1028.

(71) Barabash, S. V.; Ozolins, V.; Wolverton, C. First-Principles Theory of Competing Order Types, Phase Separation, and Phonon Spectra in Thermoelectric $AgPb_mSbTe_{m+2}$ Alloys. *Phys. Rev. Lett.* **2008**, *101*, 155704.

(72) Barabash, S. V.; Ozolins, V.; Wolverton, C. First-principles theory of the coherency strain, defect energetics, and solvus boundaries in the PbTe-$AgSbTe_2$ system. *Phys. Rev. B* **2008**, *78*, 214109.

(73) Schröder, T.; Rosenthal, T.; Giesbrecht, N.; Nentwig, M.; Maier, S.; Wang, H.; Snyder, G. J.; Oeckler, O. Nanostructures in Te/Sb/Ge/Ag (TAGS) Thermoelectric Materials Induced by Phase Transitions Associated with Vacancy Ordering. *Inorg. Chem.* **2014**, *53*, 7722–7729.

(74) Shafeie, S.; Guo, S.; Hu, Q.; Fahlquist, H.; Erhart, P.; Palmqvist, A. High-entropy alloys as high-temperature thermoelectric materials. *Journal of Applied Physics* **2015**, *118*, 184905.

(75) Kazem, N.; Zaikina, J. V.; Ohno, S.; Snyder, G. J.; Kauzlarich, S. M. Coinage-Metal-Stuffed $Eu_9Cd_4Sb_9$: Metallic Compounds with Anomalous Low Thermal Conductivities. *Chem. Mater.* **2015**, *27*, 7508–7519.

Table of Contents/Abstract graphic

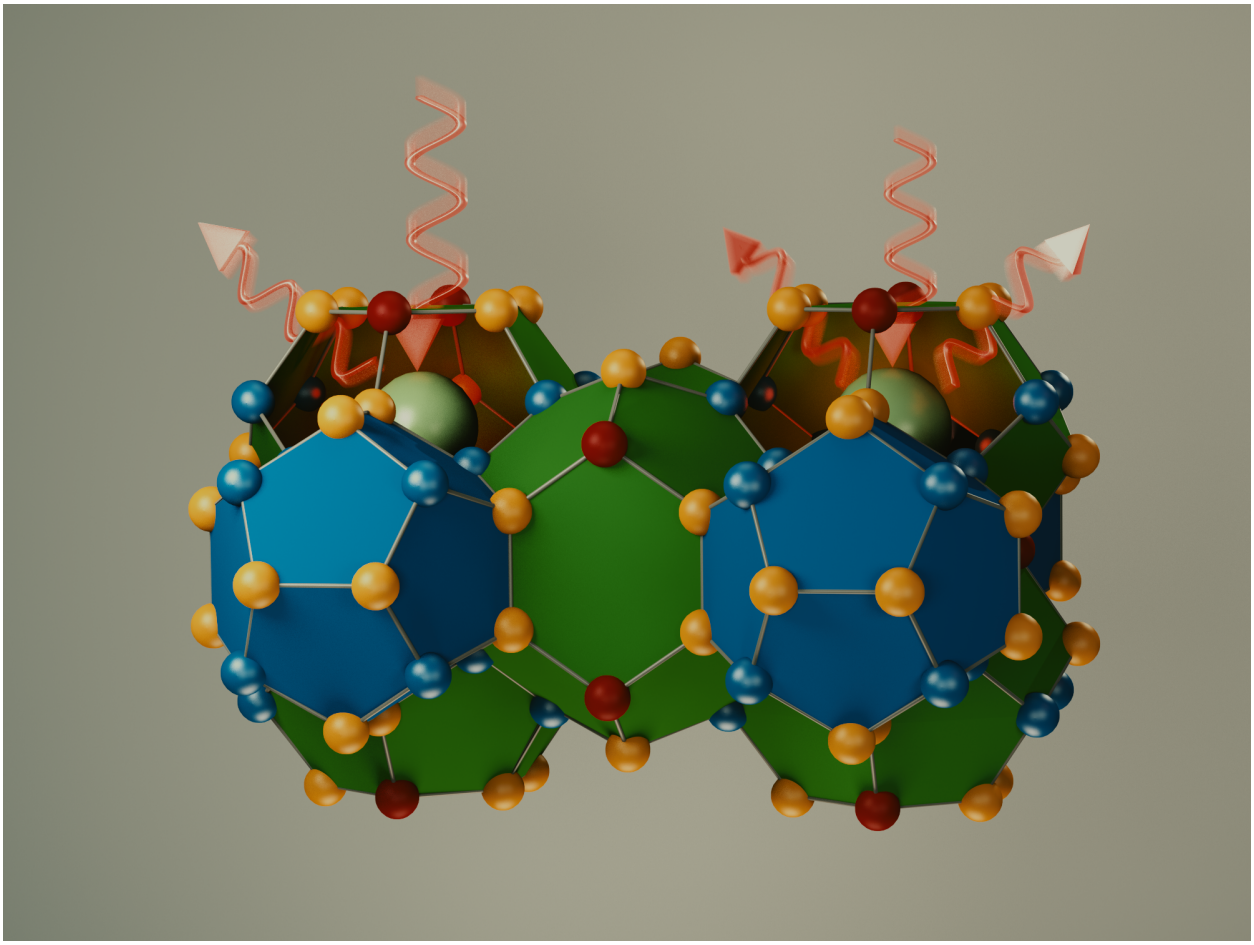

Chemical ordering patterns that yield optimal transport properties can be determined by computational design.

Supplementary information:

Optimization of the thermoelectric power factor: Coupling between chemical order and transport properties

Table S1: Comparison of special structures identified in this work. The site occupancy factors refer to space group $Pm\bar{3}n$ (ITC no. 223). The power factor was obtained under n-type conditions at 900 K and a charge carrier density of $n_e = 3 \times 10^{20}\text{cm}^3$. Results of DFT calculations using the mBJ functional are reported in brackets; all other DFT data were obtained using the PBE functional.

Configuration		Ground state		Power factor optimized	
Site occupancy factors (%)	$6c$	50		0	
	$16i$	6.25		25	
	$24k$	50		50	
		CE	DFT	CE	DFT
Total energy (eV/cell)		−215.05	−215.13	−214.70	−214.72
Band gap (eV)		0.49	0.54 (0.78)	0.50	0.55 (0.83)
Power factor (μW/K^{2}cm)		16.5	14.2	24.2	27.0

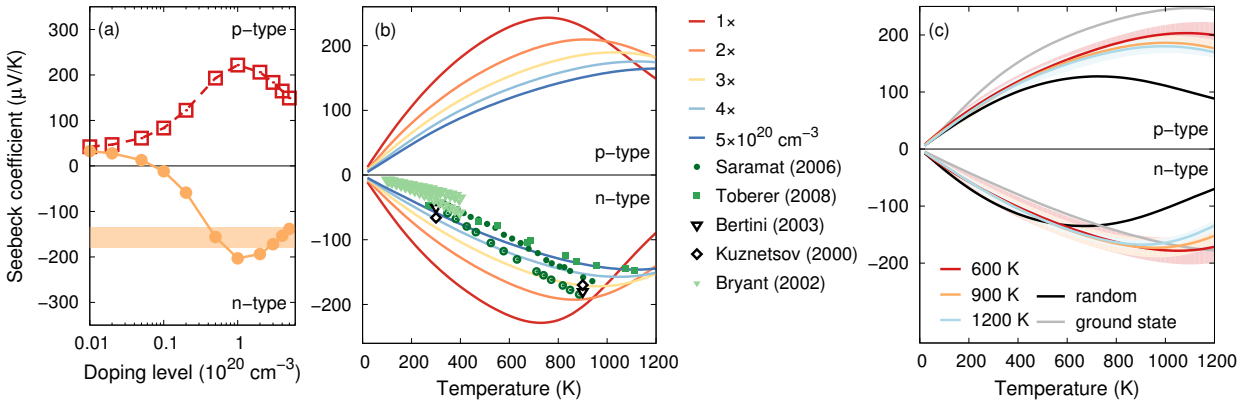

Figure S1: Seebeck coefficient S. (a) Dependence of S on the charge carrier concentration at 900 K. The shaded area represents the range of experimental values.[41,42,44] (b) Seebeck coefficient for different charge carrier densities when averaged over all representative MC structures. (c) Seebeck coefficient of p and and n-type material at a charge carrier density of $3 \times 10^{20}\,\text{cm}^{-3}$ for different structures.

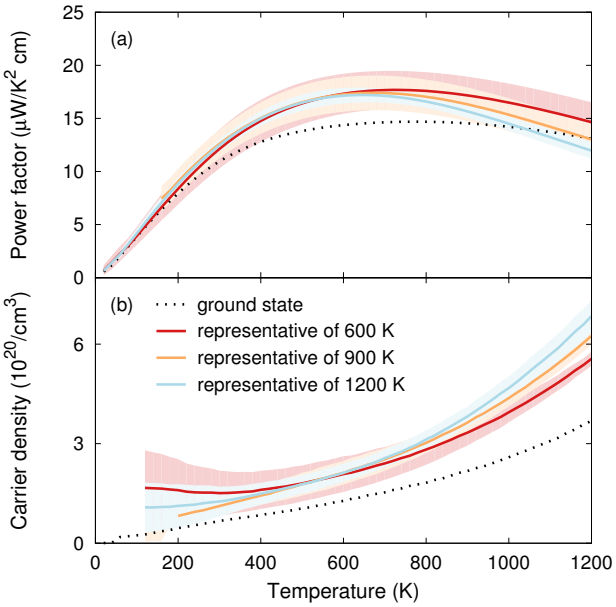

Figure S2: Maximal power factor for n-type material. For each configuration and temperature the power factor (a) was maximized with respect to charge carrier density (b) using the lifetime parameter established previously $\tau_{300} = 1.5 \times 10^{-14}\,\mathrm{s}$.

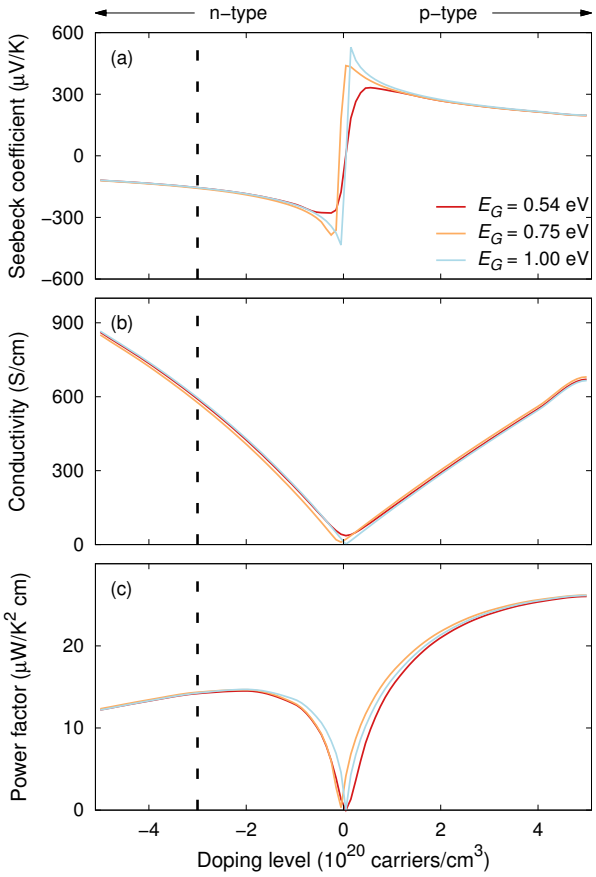

Figure S3: Dependence of transport properties on band gap for the fully ordered ground state structure. Negative doping levels (charge carrier concentrations) indicate n-type doping. The vertical dashed lines indicate the doping level of $n_e = 3 \times 10^{20}\,\mathrm{cm}^{-3}$ used throughout the major part of the present work. The band gap calculated by DFT-PBE calculations is 0.54 eV (red lines). For the other two cases ($E_G = 0.75\,\mathrm{eV}$, orange line; $E_G = 1.0\,\mathrm{eV}$, blue line) the band gap was increased by rigidly shifting all conduction band upward (scirssors correction). Note that for doping levels $|n_{e,h}| > 10^{20}\,\mathrm{cm}^{-3}$, which correspond degenerately to doped material, the transport properties are almost independent of the band gap.

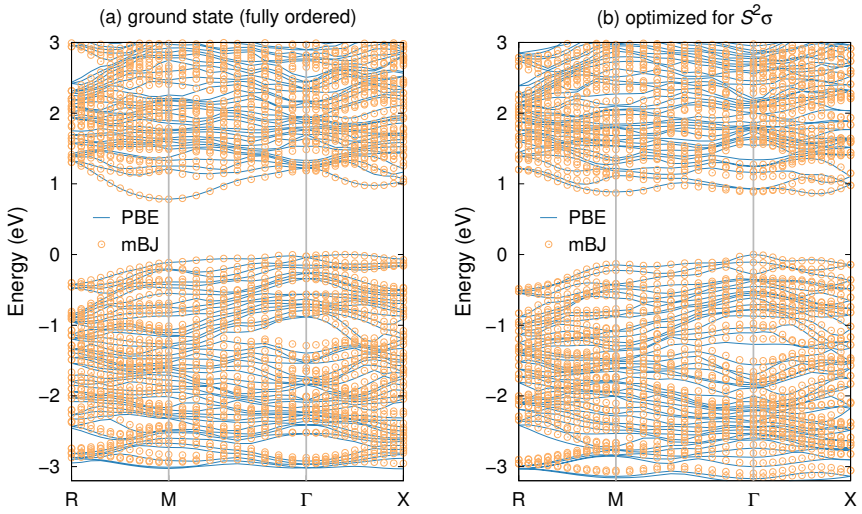

Figure S4: Band structures for the (a) ground state structure and (b) the power factor optimized structure from PBE-DFT and mBJ-DFT calculations. The conduction band edge of the PBE-DFT band structure was rigidly shifted upward to match the conduction band minimum of the mBJ-DFT data. Note that apart from the difference in band gap (also compare Table S1) the two exchange-correlation functionals yield almost identical band structures (and thus group velocities) in the region that determines the near-equilibrium transport properties of interest in the present work.

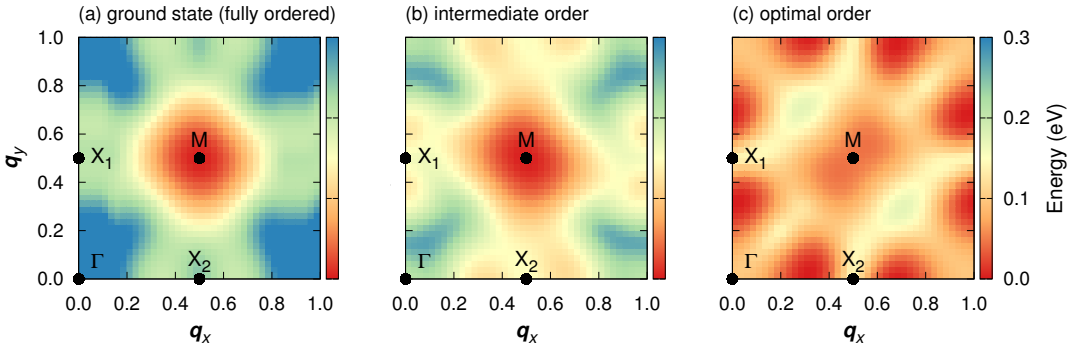

Figure S5: Energy of the lowermost conduction band relative to the conduction band minimum for (a) the fully ordered ground state, (b) a configuration with intermediate order extracted from a MC simulation, and (c) the structure optimized for maximum power factor at 900 K. Also compare the band structures shown in Fig. 6.

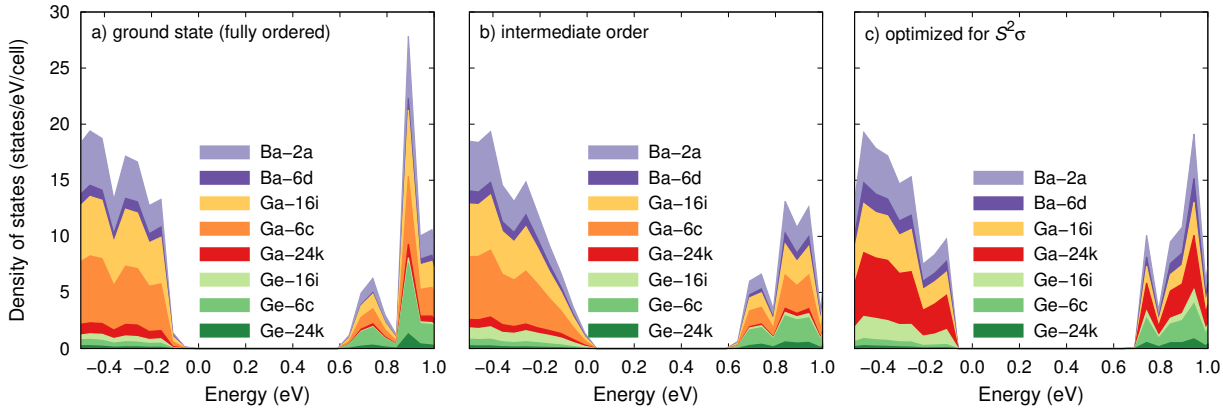

Figure S6: Partial density of states for (a) the fully ordered ground state, (b) a configuration with intermediate order extracted from a MC simulation, and (c) the structure optimized for maximum power factor at 900 K. The energy scales for the different configurations were aligned using the Ba-1*s* states as in Fig. 6.

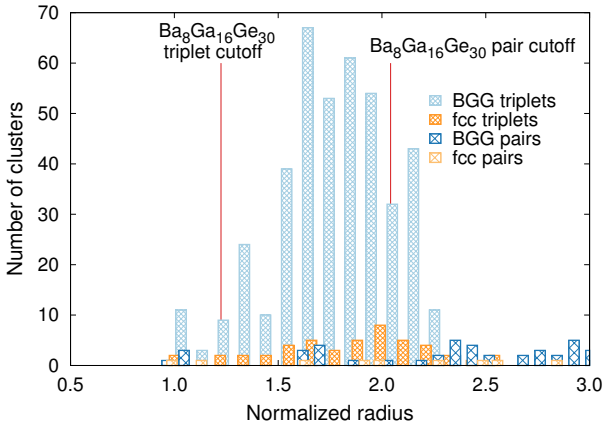

Figure S7: Number of effective cluster interactions (ECIs) as a function of cluster radius for the inorganic clathrate structure considered in the present work and a face-centered cubic (fcc) crystal.

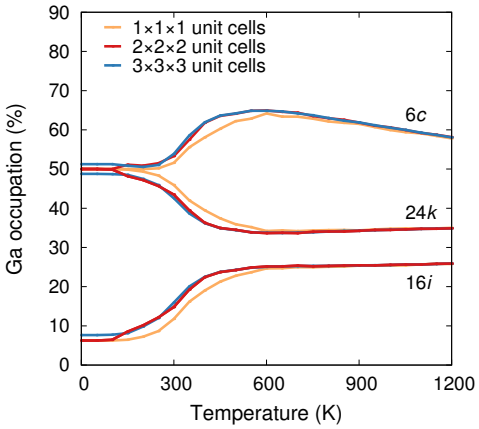

Figure S8: Effect of supercell size on temperature dependence of site occupancy factors (SOFs). Note that the overall effect is rather small. In the case of the $3 \times 3 \times 3$ supercell the system did not fully reach the ground state as evident from the deviation from the ideal zero K SOFs and a larger energy per unit cell.